



Ultrastructural Analysis of Thalamus Damages in a Mouse Model of Osmotic-Induced Demyelination

Joanna Bouchat¹ · Jacques Gilloteaux^{1,2} · Valérie Suain³ · Daniel Van Vlaender¹ · Jean-Pierre Brion³ · Charles Nicaise¹ 

Received: 25 July 2018 / Revised: 25 March 2019 / Accepted: 4 April 2019 / Published online: 2 May 2019
© Springer Science+Business Media, LLC, part of Springer Nature 2019

Abstract

A murine model used to investigate the osmotic demyelination syndrome (ODS) demonstrated ultrastructural damages in thalamus nuclei. Following chronic hyponatremia, significant myelinolysis was merely detected 48 h after the rapid reinstatement of normonatremia (ODS 48 h). In ODS samples, oligodendrocytes and astrocytes revealed injurious changes associated with a few cell deaths while both cell types seemed to endure a sort of survival strategy: (a) ODS 12 h oligodendrocytes displayed nucleoplasm with huge heterochromatic compaction, mitochondria hypertrophy, and most reclaimed an active NN cell aspect at ODS 48 h. (b) Astrocytes responded to the osmotic stress by overall cell shrinkage with clasmotodendrosis, these changes accompanied nucleus wrinkling, compacted and segregated nucleolus, destabilization of astrocyte-oligodendrocyte junctions, loss of typical GFAP filaments, and detection of round to oblong woolly, proteinaceous aggregates. ODS 48 h astrocytes regained an active nucleus aspect, without restituting GFAP filaments and still contained cytoplasmic proteinaceous deposits. (c) Sustaining minor shrinking defects at ODS 12 h, neurons showed slight axonal injury. At ODS 48 h, neuron cell bodies emerged again with deeply indented nucleus and, owing nucleolus translational activation, huge amounts of polysomes along with secretory-like activities. (d) In ODS, activated microglial cells got stuffed with huge lysosome bodies out of captures cell damages, leaving voids in interfascicular and sub-vascular neuropil. Following chronic hyponatremia, the murine thalamus restoration showed macroglial cells acutely turned off transcriptional and translational activities during ODS and progressively recovered activities, unless severely damaged cells underwent cell death, leading to neuropil disruption and demyelination.

Keywords Osmotic demyelination syndrome · Astrocytopathy · Oligodendrocytopathy · Clasmotodendrosis

Abbreviations

ΔSNa^+ Gradient of serum Na^+
BBB Blood-brain barrier

CNS Central nervous system
GFAP Glial fibrillary acidic protein
HN Hyponatremic

Joanna Bouchat and Jacques Gilloteaux contributed equally to this work.

Electronic supplementary material The online version of this article (<https://doi.org/10.1007/s12640-019-00041-x>) contains supplementary material, which is available to authorized users.

✉ Charles Nicaise
charles.nicaise@unamur.be

Joanna Bouchat
joanna.bouchat@unamur.be

Jacques Gilloteaux
jacques.gilloteaux@unamur.be

Valérie Suain
vsuain@ulb.ac.be

Daniel Van Vlaender
dvanvlaender@unamur.be

Jean-Pierre Brion
jpbrion@ulb.ac.be

¹ Unité de Recherche en Physiologie Moléculaire (URPhyM) – NARILIS, Faculté de Médecine, Université de Namur, Rue de Bruxelles 61, B-5000 Namur, Belgium

² Department of Anatomical Sciences, St George's University School of Medicine, Newcastle upon Tyne, UK

³ Laboratory of Histology, Neuroanatomy and Neuropathology, Université Libre de Bruxelles, Brussels, Belgium

NN	Normonatremic
ODS	Osmotic demyelination syndrome
RER	Rough endoplasmic reticulum
SER	Smooth endoplasmic reticulum
TEM	Transmission electronic microscopy
VPL	Ventral posterior lateral
VPM	Ventral posterior medial

Introduction

Regional susceptibility to degeneration remains elusive for osmotic demyelination syndrome (ODS). This disease is characterized by pattern-specific centropontine and extrapontine lesions (Adams et al. 1959), developing secondary to abrupt changes in plasma osmolarity (Tomlinson et al. 1976). Based on the paradigm of a rapid correction of chronic hyponatremia, animal models develop pathognomonic lesions in pontine nuclei, thalamus nuclei, cerebral cortex layers, and other subcortical structures, resembling those found in human pathology (Illowsky and Laurenco 1987; Kleinschmidt-DeMasters and Norenberg 1981; Laurenco 1983; Verbalis and Drutarosky 1988). The etiology of ODS is complex and likely involves the inability of brain glial cells, i.e., subtypes of oligodendrocytes and astrocytes, to adapt to rapid osmotic shifts. Evidences from experimental models tend to show that demyelination is rather a consequence of local oligodendrocyte cell death than myelin wrapping being the primary target. Intriguingly, the most myelinated tracts (e.g., corpus callosum) and the neuronal populations remain spared whereas astrocytes of lesioned areas concomitantly undergo degenerative changes (Gankam Kengne et al. 2011; Gocht and Lohler 1990; Kleinschmidt-DeMasters and Norenberg 1981; Popescu et al. 2013; Powers and McKeever 1976).

In the present report, an in-depth ultrastructural analysis of the thalamus, a brain region prone to demyelination in ODS, was conducted following a previously developed mouse model (Bouchat et al. 2018) and discussed in light of the ultrastructural findings described with regards of human case reports (Powers and McKeever 1976) and the rat model of ODS (Rojiani et al. 1994). The morphological analysis has been focused on the relay thalamic nuclei—ventral posterolateral (VPL) and ventral posteromedial (VPM)—because of their susceptibility towards osmotic-induced demyelination (Bouchat et al. 2018).

In the present paradigm, mice were experimentally subjected to chronic severe hyponatremia and then abruptly corrected. Subsequently, mice developed gliopathy as well as demyelinating lesions in the thalamus among other brain regions within 48 h post-correction. Several immunohistochemical markers indicating changes in the macroglial and microglial cells have been reviewed and extended with systematic electron microscopy investigations.

Methods

Animals

The experimental protocol was conducted in compliance with the European Communities Council Directives for Animal Experiments (2010/63/EU, 87-848/EEC and 86/609/EEC) and was approved by the Animal Ethics Committee of University of Namur (Ethic project n°14-210). Male C57Bl/6J mice, aged from 3 to 4 months, were housed in a temperature and humidity-controlled room maintained at 12:12 h light/dark cycle.

Protocol of Osmotic-Induced Demyelination

ODS was induced in mice as described previously (Bouchat et al. 2018). Briefly, an osmotic minipump (Model 1004, Alzet, Cupertino, CA, USA) filled with desmopressin acetate (0.002 mg/ml) (Minirin®, Ferring, Saint-Prex, Switzerland) was inserted subcutaneously at day 0. Standard pellets and water were replaced by a low-sodium liquid diet (AIN76A, MP Biomedicals, Santa Ana, CA, USA), for a period of 4 days ad libitum. In the 4th day, blood serum level was measured using Spotchem EL SE-1520 electrolyte analyzer (Arkray, Kyoto, Japan) and hyponatremia, as found below 124 mEq/L, was corrected by an intraperitoneal injection of hypertonic saline (NaCl 1 M; 1.5 ml/100 g body weight). At 12 and 24 h post-correction, natremia was measured to confirm the swift correction of hyponatremia. Eight mice were included in the protocol and divided into four groups (Fig. 1a): normonatremic mice (NN, $n = 2$), uncorrected 4-days hyponatremic mice (HN, $n = 2$), ODS mice sacrificed 12 h post-correction (ODS 12 h, $n = 2$), and ODS mice sacrificed 48 h post-correction (ODS 48 h, $n = 3$).

Histology and Immunohistochemistry

Under anesthesia (ketamine 100 mg/kg and xylazine 5 mg/kg), mice were transcardially perfused with NaCl 0.9% followed by phosphate-buffered 4% paraformaldehyde (PFA). Brains were separated into two hemispheres and post-fixed overnight. Left hemispheres were thereafter dehydrated and paraffin-embedded. Paraffin sections (6 μ m) were dewaxed, rehydrated, and either stained with Eriochrome Cyanine or processed for immunohistochemistry. The immunoprocessing included first a heat-induced epitope retrieval in citrate buffer pH 6 at 100 °C for 10 min. Endogenous peroxidase activity was then quenched using 3% H₂O₂ in methanol for 10 min. Non-specific binding was blocked using 5% goat or horse serum diluted in TBS for 15 min. Histologic sections were incubated overnight at 4 °C with primary antibodies diluted in TBS containing 1% normal serum: NeuN for neurons (Cell Signaling D3S3I, 1:1000); Aldh1L1 (Abcam

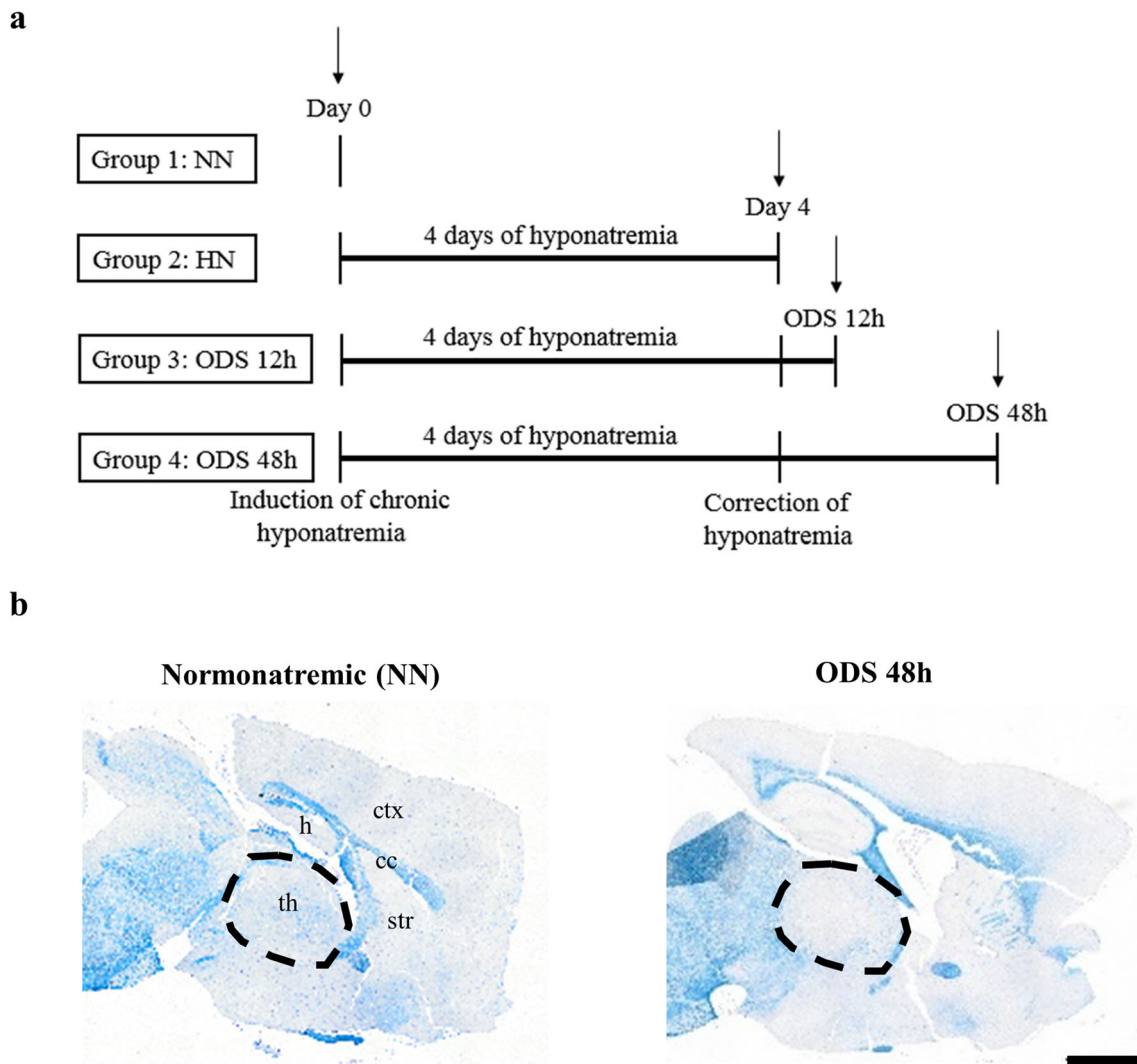


Fig. 1 Murine ODS experimental procedure leading to demyelination in thalamus nuclei. Experiments were performed on 4 groups of 2 mice excepted for ODS 48 h which included 3 mice. Normonatremic mice (NN) from group 1 were sacrificed at day 0 (arrow) while uncorrected hyponatremic mice (HN) were sacrificed 4 days after the induction of hyponatremia (arrow). ODS mice were sacrificed at 12 and 48 h post-

correction for groups 3 and 4, respectively (arrows) (a). Sagittal sections from NN (left) and ODS 48 h (right) stained with Eriochrome Cyanine confirmed demyelination at 48 h post-correction (b). Thalamus (encircled) was dissected as described in the Experimental Procedure. *cc* corpus callosum, *ctx* cortex, *h* hippocampus, *str* striatum or caudate putamen, *th* thalamus. Scale bar = 1 mm

ab87117, 1:1000) and GFAP (Sigma G3893, 1:1000) for astrocytes; and p25 α (Sigma HPA036576, 1:1000) for oligodendrocytes and Iba1 (Wako 019-19741, 1:1000) for microglial cells. The next day, sections were incubated with a biotinylated secondary antibody (1:100–Vectastain, Vector Laboratories, Burlingame, CA, USA) for 1 h at room temperature. Then, sections were incubated with a solution of peroxidase-bound streptavidin (1:100–Vectastain) for 45 min. Immunoreactivity was revealed using diaminobenzidine (Dako, Glostrup, Denmark) and hemalum was used as counterstain. Finally, dehydrated and mounted in DPX sections were observed with an Olympus BX63 microscope (Olympus, Tokyo, Japan) equipped with Olympus SC50 camera. Images were acquired with the Cell Sens Software.

Ultrastructural Aspects

Under anesthesia, mice were transcardially perfused with a solution of PFA 2% and glutaraldehyde 2% in 0.1 M phosphate buffer (pH 7.2–7.4). Right hemispheres were sliced in 1-mm sagittal sections with an Alto sagittal matrice (AgnTho's, Lidingö, Sweden). At 12 and 48 h post-correction, the thalamus was dissected (Fig. 1b) and VPM and VPL nuclei were sampled (lateral plans 1.0 to 2.0 mm from interhemispheric fissure) according to Paxinos and Franklin's mouse brain atlas. These samples were harvested using a neurological punch of 0.69 mm of internal diameter (Fine Science Tools #18036-19, Heidelberg, Germany) (Supplemental Fig. S1). At 48 h post-correction, supplemental samples were isolated from

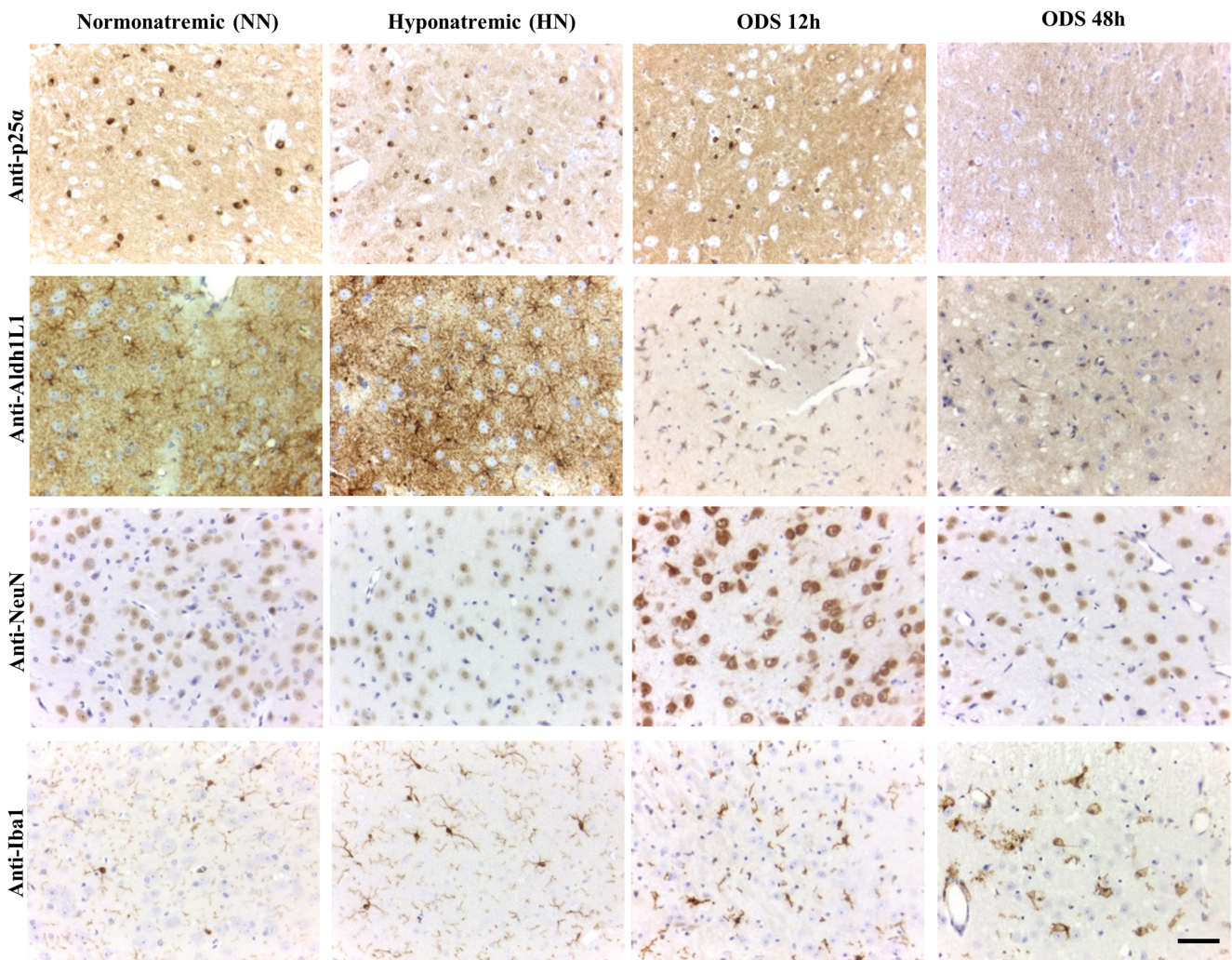


Fig. 2 Evolution of glial and neuronal cell markers during ODS. Immunolabeling of oligodendrocytes (p25 α), astrocytes (Aldh1L1), neurons (NeuN), and microglial cells (Iba1) are displayed into lines while each different group (NN, HN, ODS 12 h, and 48 h) are distributed into columns: progressive loss of immunoreactivity of

p25 α ⁺ oligodendrocytes and Aldh1L1⁺ astrocytes during ODS time points with relative NeuN sparing. Microglial cells underwent morphological changes from quiescent to activated phenotype at 48 h post-correction. Scale bar = 50 μ m

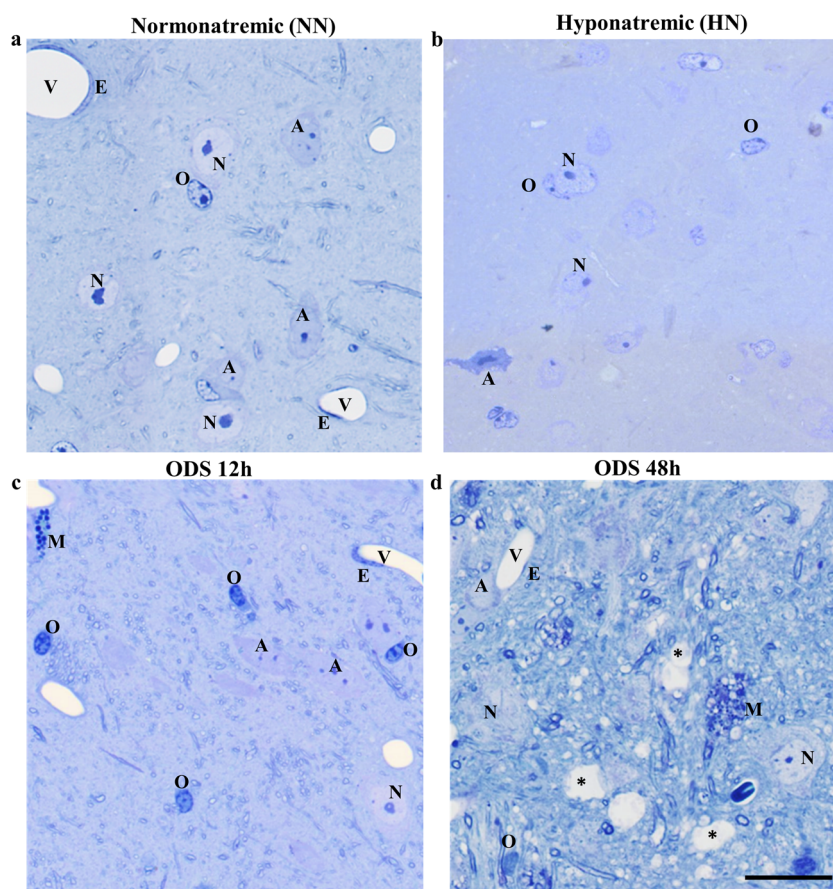
the caudate putamen and from the thalamus lesion periphery that was beforehand identified using GFAP immunolabeling. Left hemispheres were processed for myelin staining and GFAP-immunohistochemistry and used as template to delineate demyelinating lesion(s) and perilesional astrogliosis, respectively (Supplemental Fig. S1). Right hemispheres were post-fixed in glutaraldehyde 4% for 2 h. They were washed in Millonig's buffer containing 0.5% sucrose for 1 day and post-fixed in OsO₄ 2%, dehydrated and embedded in epoxy resin. Semi-thin sections (1 μ m) were stained with toluidine blue 1% in a solution of borax 2% to delineate the region-of-interest. Obtained with a diamond knife, ultrathin sections (40–70 nm) were collected on 200 and 300 mesh nickel grids (Micro to Nano, Haarlem, Netherlands) and contrasted with uranyl acetate and lead citrate. They were observed with a Philips Tecnai 10 electron microscope, at an accelerating

voltage of 60–80 kV and equipped with a digitized Olympus ITEM platform MegaView G2 image analysis.

Immunogold Labelling

Under anesthesia, mice from the condition ODS 48 h were transcardially perfused with a solution of PFA 4% and glutaraldehyde 0.25% in 0.1 M phosphate buffer (pH 7.2–7.4). Right hemispheres were sliced in 1-mm sagittal sections with an Alto sagittal matrice (AgnTho's, Lidingö, Sweden). Thalamic lesional samples were sampled and post-fixed overnight in the same fixative. Samples were dehydrated and embedded in epoxy resin. Ultrathin sections were etched with hydrogen peroxide 10% in distilled water during 10 min. Non-specific binding was blocked using 10% goat serum diluted in buffer during 30 min. Sections were incubated overnight at 4 °C with primary antibodies: GFAP (Sigma G3893,

Fig. 3 Identification of nerve cells in semi-thin thalamus sections. Comparison between 1- μ m-thick, semi-thin sections stained by toluidine blue of representative NN (a), HN (b), ODS 12 h (c), and ODS 48 h (d) mouse thalamus areas where astrocytes (A), microglial cells (M), neurons (N), oligodendrocytes (O), and blood vessels (V) lined by endothelium (E) are marked. Asterisks in ODS48h represent luminal voids which are not vascular. Scale bar = 20 μ m



1:500) and β -actin (Sigma A5441, 1:500). The second day, samples were incubated with a secondary antibody anti-mouse conjugated to 10 nm colloidal gold diluted 1:20 in buffer during 1 h before contrasting with uranyl acetate and lead citrate. Sections were observed with a Philips Tecnai 10 electron microscope. Positive controls consisting of the mouse cortex were included in this experiment.

Results

Blood Parameters during ODS Protocol

Mice included in the protocol were monitored for natremia along different timings of experimental ODS (Fig. 1a). Average natremia (mea \pm SEM) were respectively 146.6 ± 2.1 mEq/L for the normonatremic group and 118.2 ± 1.6 mEq/L for the chronic hyponatremic group. At 12 or 24 h after the correction of hyponatremia, natremia raised to 146 ± 5.1 mEq/L, with a mean Δ SNa⁺ of 34.2 ± 3.3 mEq/L.

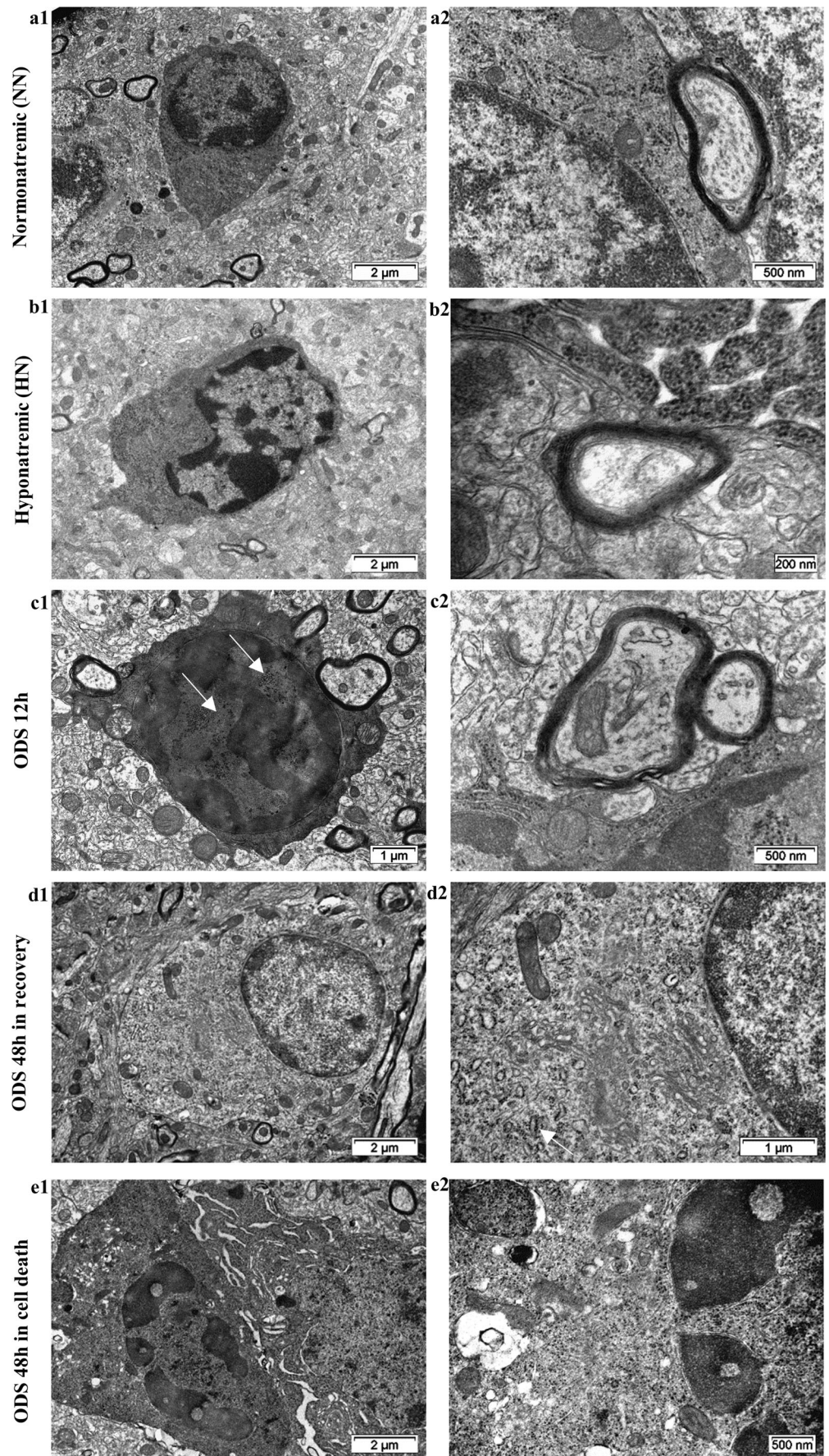
Histological Aspects of Thalamic Nervous Cells

Anti-p25 α , Aldh11, Iba1, and NeuN immunohistochemistry was applied to respectively identify oligodendrocytes,

astrocytes, neurons, and microglia on thalamus slices. While no evident cellular changes could be observed in the thalamus of chronic hyponatremic mice at light microscope examination, the brains of mice that underwent the correction of hyponatremia showed severe gliopathy with relative neuronal sparing (Fig. 2). At 12 h post-correction, the number of p25 α ⁺ cells was strikingly reduced, Aldh111⁺ cells appeared swollen with shortened processes, and Iba1⁺ cells started to change their morphology from quiescent to activated microglia. At ODS 48 h, the immunoreactivities for p25 α or Aldh111 cells appeared obliterated while activated microglia were identified by their typical amoeboid enlargement.

Representative thalamus fields of view of each sample-group, stained with toluidine blue, facilitated the identification of each cell type and changes, further examined with TEM (Fig. 3). Either interfascicular or satellite, oligodendrocytes were recognized due to their high basophilic aspect in the neuropil, between groups of myelinated fibers, or adjacent to a neuron cell body. In HN and in ODS 12 h, they demonstrated a higher nuclear contrast than in NN. However, ODS 48 h oligodendrocyte cells reappeared with a lesser contrast than that of ODS 12 h cells. Either fibrous or protoplasmic, NN astrocytes types had a cell body size ranging from 10 to 18 μ m in long diameter and 5 to 6 μ m in small diameter containing an elongated euchromatic nucleus profile with a centrally located nucleolus. A

Fig. 4 Comparative ultrastructural changes between NN, HN, ODS 12 h, and ODS 48 h thalamus oligodendrocytes. Nucleus content and cytoplasm characteristics of NN (a1, a2) are compared with chromatin and nucleolus compactions in HN (b1, b2), mottled hyperchromaticity (c1, c2) with granules resembling interchromatin granules in ODS 12 h (c1, arrows), and either an apparent recovery of transcription (reallocation of ribosomes to RER membranes and obvious Golgi apparatus) in most cells of ODS 48 h (d1, d2), while some axoplasm and myelin worsen their damages and rare cases of cell death are revealed (e1, e2)



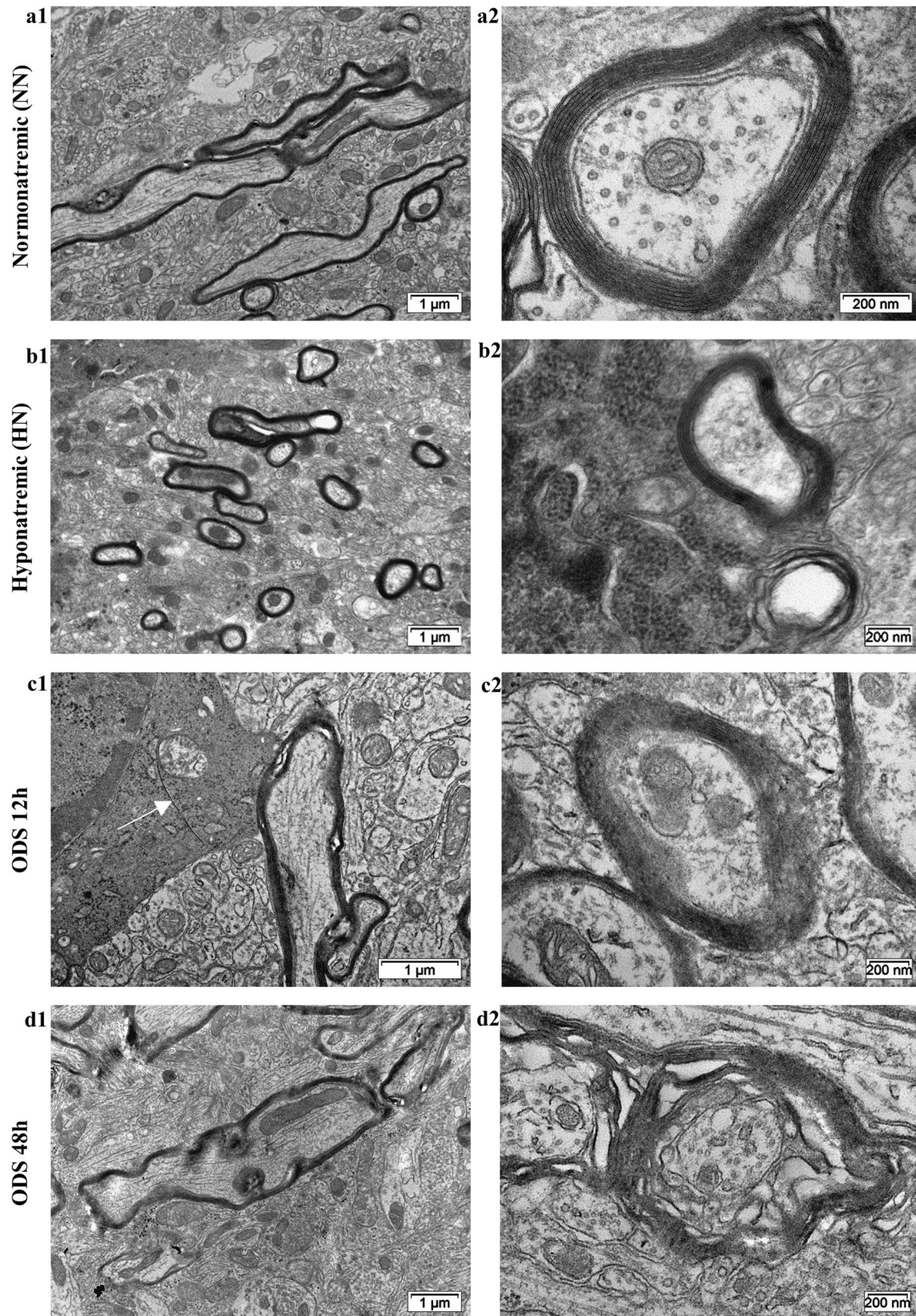
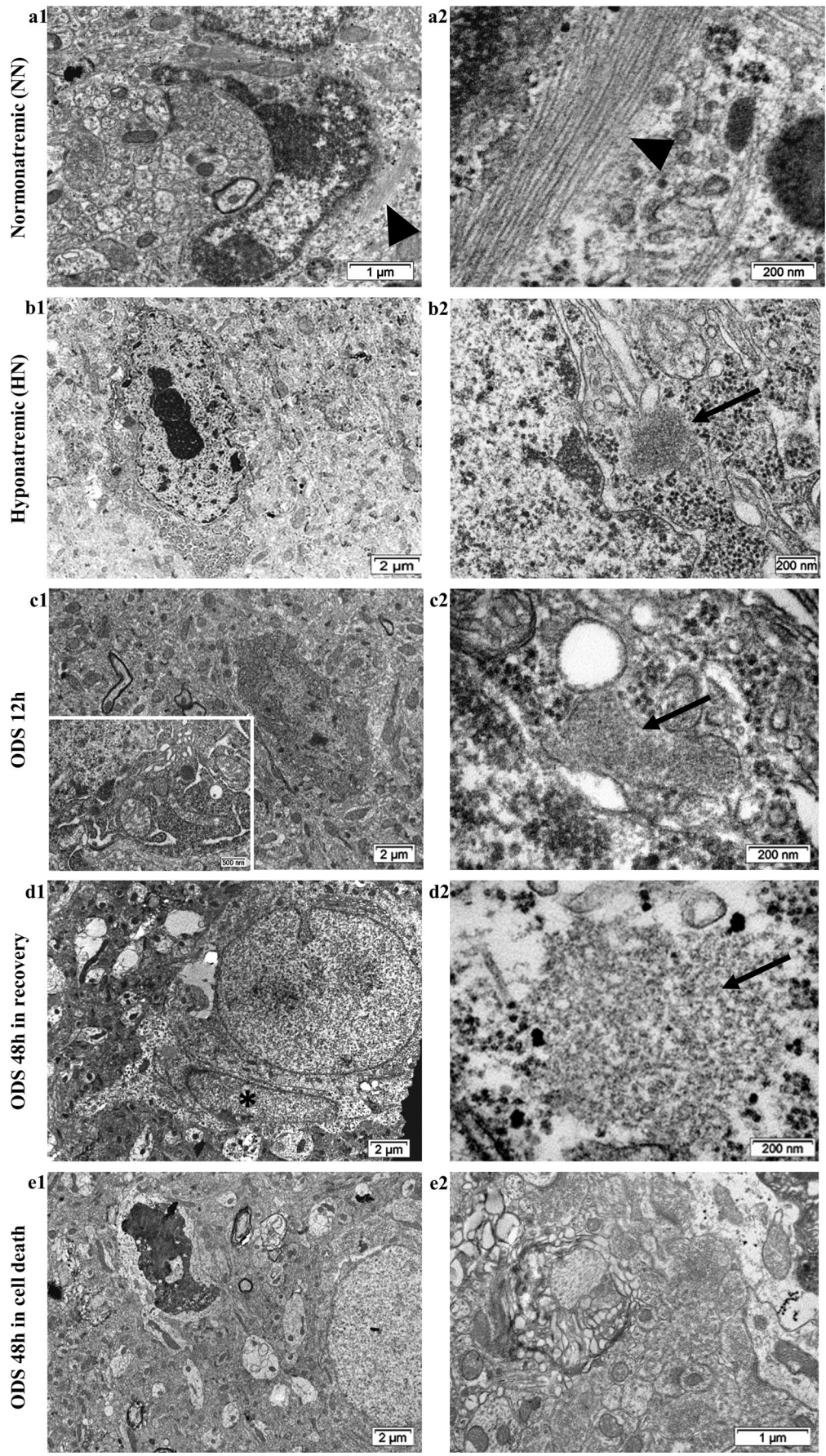


Fig. 5 Representative ultrastructural aspects of NN, HN, ODS 12 h, and ODS 48 h thalamus myelinated axons. Compared with the NN group (a1, a2), myelin damages can be noted to increase from HN (b1, b2) to ODS 12 h (c1, c2) and 48 h (d1, d2) in the sequence ODS 48 h > ODS 12 h >

HN. Associated oligodendrocyte changes can be noted caused by osmotic shock, i.e., phagosome built near altered mitochondria (c1, arrow) and myelin protrusions into foamy, adaxonal degradations (d1, d2)



◀ **Fig. 6** Representative ultrastructural aspects of NN, HN, ODS 12 h, and ODS 48 h thalamus astrocytes. Only protoplasmic NN cells display typical GFAP bundles in the perikaryon (a1, a2, arrowheads) while HN (b1, b2), ODS 12 h (c1, c2), and ODS 48 h (d1, d2) astrocytes reveal nucleus content changes along with contrast and small to large aggregates of fibrous precursors (arrows) amidst variable amounts of polyribosomes and glycogen reserve. Enlargement in c1 showed swollen organelles at 12 h post-correction. Most ODS 48 h cells retrieve euchromatic aspect (d1, asterisk) and beta-glycogen left out of glycolysis (d2). Some rare events of cell death ensue, again with leftover glycogen, marking astrocytes (e1–e2)

faint pinkish metachromatically stained cytoplasm appeared due to their glycogen load. A more basophilic contrast appeared in HN and ODS 12 h since cell shrinking seems to have compressed and elongated the cells while the extracellular space was vacuolated; the wrinkled nucleus verified this shrinkage phenomenon. At ODS 48 h time point, most astrocytes regained the NN lesser stainability and morphology. In all groups, neurons were identified as the largest cells containing a pale-stained but well delineated, *quasi* round nucleus and a central, well-contrasted nucleolus. In NN neurons, the nucleus is also clearly indented which disappears in HN and ODS 12 h while nucleolus increased in size. At ODS 48 h time, deep nucleus indents can be found again with a marked basophilic neuroplasm. They were frequently accompanied by a satellite oligodendrocyte and, in some lucky views, with also an associated astrocyte. Neuropil component revealed some spongy aspect with luminal voids that was not vascular in ODS 48 h (Fig. 3d, asterisks). In both NN and HN, microglial cells were difficult to recognize on toluidine-stained semi-thin sections. However, in ODS 12 and 48 h, they became identifiable due to the expanded size by containing loads of darkly, blueish lysosomal bodies. At ODS 48 h, the amount of debris allowed to view them among the neuropil containing interfascicular and sub-vascular voids resulting from their macrophagic activities.

Transmission Electron Microscopy Findings

Oligodendrocytes

NN Oligodendrocytes Oligodendrocytes, whether interfascicular or satellite to neurons, were easily recognized out of the neuropil and among other cell types because of their small size (ranging from 4.5 to 6.5 μm in diam.) and an overall high electron contrast (Fig. 4a1). In NN sections, the electron-contrasted cell bodies typically showed round to pear shape and contained an oval to round eccentric nucleus and a narrow perikaryon. The evident euchromatic nucleus along with its nucleolus suggested a cell with high activity because all the typical organelles were recognized in this narrow perikaryon, especially the Golgi apparatus and circumferential saccules of rough endoplasmic reticulum (RER) in a busy cytoplasm decorated by polyribosomes, short-sized mitochondria, numerous microtubules, and their centrosome. Adjacent axons, well-

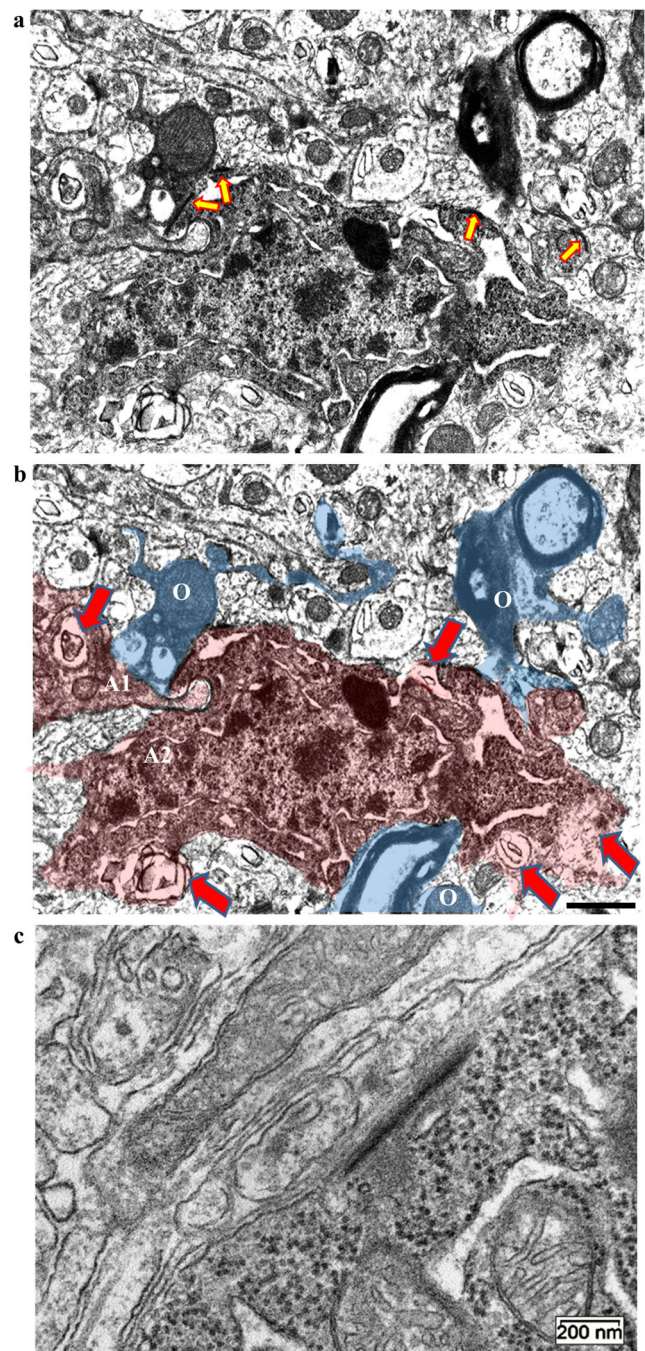


Fig. 7 Representation of thalamic astrocytes/oligodendrocytes junctions' at 12 h post-correction. An example of ODS 12 h adjacent electron-contrasted astrocytes (A) of the mouse thalamus highlighting specialized contacts (yellow arrows) with oligodendrocyte(s) (O) (a). The same micrograph of featuring astrocytes manually highlighted red with distal extensions removal characteristic of astrocytic clasmatodendrosis (red arrows). Oligodendrocyte pieces among the adjacent demyelinating neuropil are highlighted in blue. Note the peculiar heterochromatin packet's distribution alongside the dilated nucleus envelope and its extended endoplasmic reticulum; a huge contrasted lysosomal body is noted (b). High magnified view of one specialized astrocyte membrane contact zone with an adjacent filamentous aggregate among innumerable, dispersed, and admixed particulate polyribosomes and glycogen (c). Scale bars equal 1 μm in (b) and 200 nm in (c)

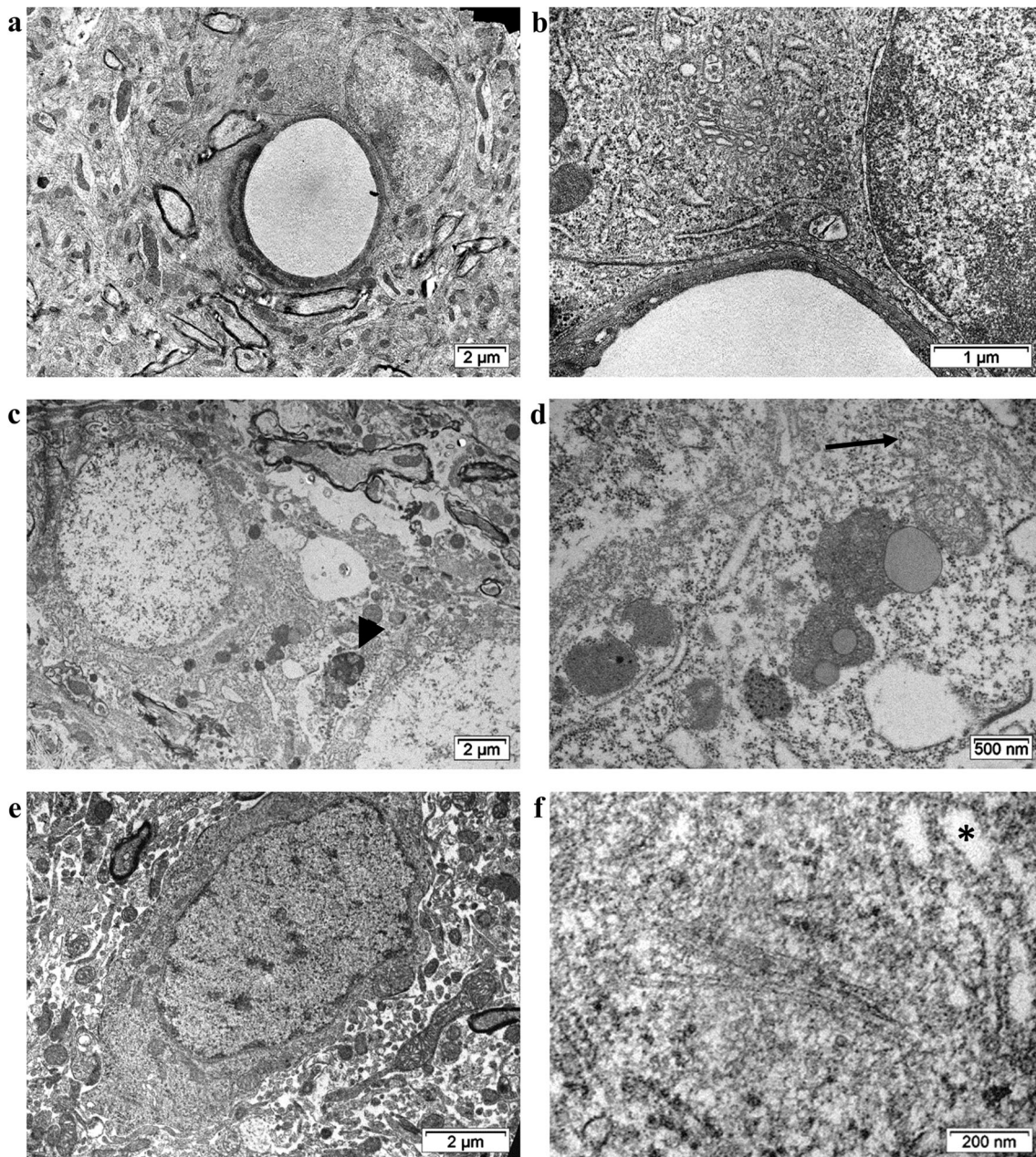


Fig. 8 Comparison between astrocytes at 48 h post-correction. Recovery astrocytes located in the thalamus lesion presented euchromatic nucleus and a cytoplasm containing swollen organelles but no intermediate filaments (**a** and **b**). Encircling reactive astrocytes showed dilated, euchromatic-like nuclei (**c**) along with lipofuscin bodies, vacuolated endoplasmic reticulum; adjacent corpses or cell debris of degraded oligodendrocyte were also observed (arrowhead in **c**). Poorly outlined

dilations of both rough and smooth endoplasmic reticulum were seen along with some chaos in their cytoskeletal and intermediate filaments that remained hard to be identified (arrow in **d**). An example of one striatum astrocytes was illustrated, showing large euchromatic nucleus with its heterochromatin (**e**) with a cytoplasm filled with barely swollen endoplasm (asterisk in **f**) among dispersed, heavy particulate glycogen and recognizable glial intermediate filaments (**f**)

circumscribed by their compacted layers of myelin, contained profiles of mitochondria, smooth endoplasmic reticulum (SER), and microtubules (Fig. 4a2).

HN Oligodendrocytes Oligodendrocytes undergoing hyponatremia displayed altered shape compared with NN ones, as their homeomorphism suggested an elongation into

quasi lozenge shape with central distorted nucleus displaying a compacted, round nucleolus, with distant heterochromatin, compatible with poor transcription and accumulation of RNA precursor's and overload accompanied by osmotic swelling (Fig. 4b1). The associated axons were circumscribed by myelin that showed rare and discrete unwrapping (Fig. 4b2).

ODS 12 H Oligodendrocytes Following correction of hyponatremia, oligodendrocytes could easily be found throughout the tissue samples because of their accentuated chromaticity. In all cells, not only nucleus but also cytoplasm was more contrasted than NN and HN oligodendrocytes. The heterochromatin compaction filled a large part of the nucleoplasm while the remaining nucleoplasm was contrasted with a mottled, grayish, and grainy appearance wherein an eventual loose but still contrasted nucleolar mass could eventually be recognized along with dispersed, coarse irregular spread of highly contrasted interchromatin granules (Fig. 4c1, arrows). Nuclear pores appeared as enlarged, electron-lucent spaces with surrounding areas as if sieve holes have been poked across the broadened, thick content of the heterochromatin background. Perikaryal zones and the flimsy extensions in the neuropil contained obvious, inflated mitochondria profiles and segments of the RER where ribosomes could be on or near the ER membrane, hanging by their mRNA treads. The mitochondria profiles could reach at least twice the size of the NN or HN ones. Adjacent axons displayed unwrapped segments, dilated and stretched damaged mitochondria, along with altered endoplasmic reticulum, lysosomal bodies, and some vacuolated content while some axo-dendritic connections were found in the vicinal neuropil. (Fig 4c2). Interestingly, random sections of the perikaryal cytoplasm showed at least one evident phagophore membrane formation along with a few grouped or loosely dispersed vacuoles (50–250 nm in diameter) with a peculiar, rimmed, interrupted electron contrast (Fig. 5c1, arrow). Lysosome bodies or even small round, heterogeneous, wrapped contrasted bodies resulted out of autophagocytotic activities.

ODS 48 H Oligodendrocytes Most fibrillar and satellite oligodendrocytes were both recognized and appeared with lower electron contrast than those of NN, HN, and ODS 12 h since both nucleus and cytoplasm appeared changed into “secretory-like” cells (Fig. 4d1). There, sections of main cell nucleated bodies revealed round to oval euchromatic, typical subcentral nucleus containing little peripheral heterochromatin, one or more nucleolus body, made of loosely contrasted components among the large, pale active nucleoplasm contrasting with the ODS 12 h oligodendrocyte ones. The perikaryon was filled with evident active organelles (Fig. 4d2) resulting from transcription and translation activities: many long and small roundish saccules of RER with fuzzy content were accompanied by an obvious Golgi apparatus of large series of cistern stacks that made mitochondria and tiny lysosome-like bodies to relocate in the outskirts of the cell. Most mitochondria profiles had regained similar morphology as those viewed in NN cells and only a few of them possessed swollen or blemished parts, as if reminding the investigator of their past osmotic “scar” defects.

Out of 20 grid fields of view, one single oligodendrocyte underwent a process of cell injury and death, not resembling apoptosis, as observed in Fig. 4e1. This cell demise encompassed a nuclear degradation that included huge compacted heterochromatin masses and nucleoplasm granular remnants surrounded by nucleus envelope remnants and finer cell debris (Fig. 4e2). This rare lethal event was surrounded by neuropil enormous myelin whorls and other fatty debris contributing in fragilization of tiny areas of the ultrathin sections.

Axons adjacent to the oligodendrocytes still showed myelin with small damages and with altered organelles (Fig. 4d1). However, those distant, among the neuropil, especially closest to surrounding blood vessels appeared with large foamy aspect, unwrapped, and with lysosomes and onion bodies (see Fig. 9 ODS 48 h). Meanwhile, adjacent myelinated axons could still be viewed with damage, where local swollen content create regional swellings along the nerve fibers (Fig. 5d1, d2).

Neuropil

Dispersed as single or small fascicles in the neuropil, NN and HN axons showed with longitudinal, oblique or cross-section views, whether the node of Ranvier could be seen or not in the same fields of view, a typical myelination where the layering was tight with axoplasm containing microtubules, mitochondria profiles, and bits of endoplasmic reticulum (ER) (Fig. 5a1, a2 for NN and 5b1, b2 for HN).

Myelinated axons of ODS 12 h thalamus displayed small disruptions that encompassed small to wide interlamellar, local unwinding aspects. These decompactions revealed either an adaxonal membrane with irregular diameter, and some small sectors of notches of smudged-like myelin notches along with internal splits (Fig. 5c1, c2). Inasmuch myelin damages accompanied many recognizable axo-dendritic connections in the neuropil, some swollen dendrites where ER was dilated and microtubule parts appeared degraded while other dendrite cross-section appeared intact after ODS 12 h and still received synaptic contacts revealed by accumulations of presynaptic vesicles, also showing their postsynaptic density specializations.

At ODS 48 h, demyelination progression provoked frothy aspects surrounding the remained axon that underwent swelling and degradations noted by whorls and lysosomal bodies within the abaxonal extensions of the oligodendrocytes. The terminal areas of few afferent axons in the thalamic areas surrounding defects were revealed by typical aggregates of synaptic vesicles facing the specialized postsynaptic membranes; other organelles, such as mitochondria and ER, and small autophagosomes filled the presynaptic parts (Fig. 5d1, d2). Often adjacent to some blood vessels degenerated axons were seen along with adjacent astrocyte remnants. There, organelles were rare or not viewed but scattered glycogen granules. Demyelinating axons were revealed as swollen aspects

or merely viewed as uncharacteristic, hollowed spaces with disengaged or concentric membrane whorls among the interfascicular neuropil.

Astrocytes

NN Astrocytes Both fibrous and protoplasmic astrocytes were ovoid cells and contained a large oval to reniform, euchromatic nucleus. The fibrous type was easily identified by abundant bundles of glial fibrillar acidic proteins (GFAP) (Fig. 6a1, a2, arrowheads). Among all the typical organelles, elongated or branching-like narrow mitochondria and a few lysosomal bodies were noted along with dispersed glycogen accumulations, mainly alpha particles. Protoplasmic astrocytes and extensions were also containing a large oval nucleus but rarely detectable GFAP filaments; they were typically adjacent to the endothelial cells or interposing pericytes.

HN Astrocytes Comforting the views obtained with light microscopy, HN astrocytes were more easily identified among the nucleated cells of the thalamus than NN ones because of their increased electron contrast cytoplasm and their highly compacted nucleolus dissociated (Fig. 6b1). Additionally, HN cells displayed a more contrasted cytoplasm than NN cells due to their high content in ribosomes mostly freed from the dilated endoplasmic reticulum and, if some remained attached, it was with empty but dilated. The dilation of this endoplasm was distinctive in HN cells because after processing, it appeared as if dissecting the cells into networks of cavities in the shape of elongated hollows. The mitochondria revealed some undulating cristae among the dilated matrix. Small Golgi apparatus was adjacent to the nucleus and one or more large, compacted lysosomal bodies were seen. The tenuous astrocyte extensions were difficult to distinguish among the changed neuropil unless some content of dispersed beta-glycogen dense particles was detected next to small aggregates of fibrous precursors (Fig. 6b2, arrow). Both HN and ODS 12 h nucleus profiles were deformed, wrinkled with an exaggerated perinuclear space while most of the euchromatic nucleoplasm contains dispersed heterochromatic packets like chromocenters (ranging from 50 to 75 nm in diam.) and located along the folded internal envelope.

ODS 12 H Astrocytes Most ODS 12 h astrocytes seemed oblong whose cytoplasm bore even higher electron contrast than HN ones. This contrast was accompanied by a prominent dilated perinuclear space, extension of the endoplasmic reticulum that appeared as wide gashes or gullies-like. This contrast and peculiar spacings caused by the osmotic correction and processing evidenced the wrinkled nucleus whose nucleoplasm contained a central, small compact nucleolus. There, roundish heterochromatin packets decorated the inner folds of the envelope (Fig. 6c1). There was no organized bundling

of intermediate filaments in ODS 12 h astrocytes. Instead, most of the time, one or more amorphous proteinaceous accumulation (ranging from 150 to 500 nm in diameter) was revealed adjacent to the other organelles, including scattered microtubules, in all the ODS 12 h astrocyte perikaryon examined (Fig. 6c2, arrow). Simultaneously, cells also comprised at least one perikaryon elongated, contrasted fibrous body that reached a width of several micrometers and the astrocyte's extensions contained damaged endoplasmic cisterns, freed of ribosomes. These changes rendered the cell extensions tenuous. Carefully outlined or in other fields of view, the astrocytes also contained dispersed, densely contrasted particles of β -glycogen granules (20–65 nm diameter); they underwent changes that involved autolytic activities: membrane whorls and other complex cytoplasm figures exposing autophagocytosis while beading these extensions comforted irreversible astrocyte injury illustrating clasmotodendrosis (Fig. 7a–b). The same Fig. 7a and its attached color-highlighted same view in Fig. 7b demonstrated such self-excising defect while preserving the perikaryon. Concurrently, an example of astrocyte-astrocyte junction as well as junction's changes of the astrocyte with adjacent oligodendrocytes was recognized in Fig. 7a and were exemplified and enlarged in Fig. 7c. This is an unusual astrocyte-oligodendrocyte junction change because the normally contacting membranes became distant and unilateral, as astrocytic submembrane deposits were shown in the adjacent zones, and appeared as in adhering junctions (Fig. 7a, arrows and c).

ODS 48 H Astrocytes from Demyelinating Lesion Most ODS 48 h astrocytes in the thalamus lesion appeared with a slightly reniform or with indented oval to round electron pale, euchromatic-like nucleus saved a few heterochromatin inner envelope packets and a nucleolus with loosen aspect with a small granular body suggestive of very active cells (Fig. 6d1, asterisk). Such astrocyte's morphology astonishingly reminded us that of NN astrocytes with lesser heterochromatin. The perikaryon contained organelles and one or more clumps of mixed fibrillary granular aggregates, 0.4 to 1 μ m diameter. Anti-GFAP or anti-actin immunogold labelling did not permit us to detect an immunoreactivity towards these cytoskeleton elements within the intracytoplasmic aggregates (data not shown). Cytoplasm was filled with ribosomes and disseminated highly contrasted β -glycogen granules

Fig. 9 Comparisons between thalamus protoplasmic astrocyte end feet before and during ODS. NN and HN end feet next to blood vessels contained typical organelles (i.e., mitochondria, RER, and glycogen) but with injurious osmotic changes denoted in HN glia limitans and surrounding cells. ODS 12 h astrocytes showed degraded organelles and lysosomes with dispersed glycogen particulates characterized by glycolytic activities. In ODS 48 h, glia limitans astrocytes, recognized by end feet where accumulated packed filaments (pointed by arrow) were found, contained adjacent huge voids and vacuoles formed by adjacent demyelinating fibers of sub-vascular zones. V blood vessels

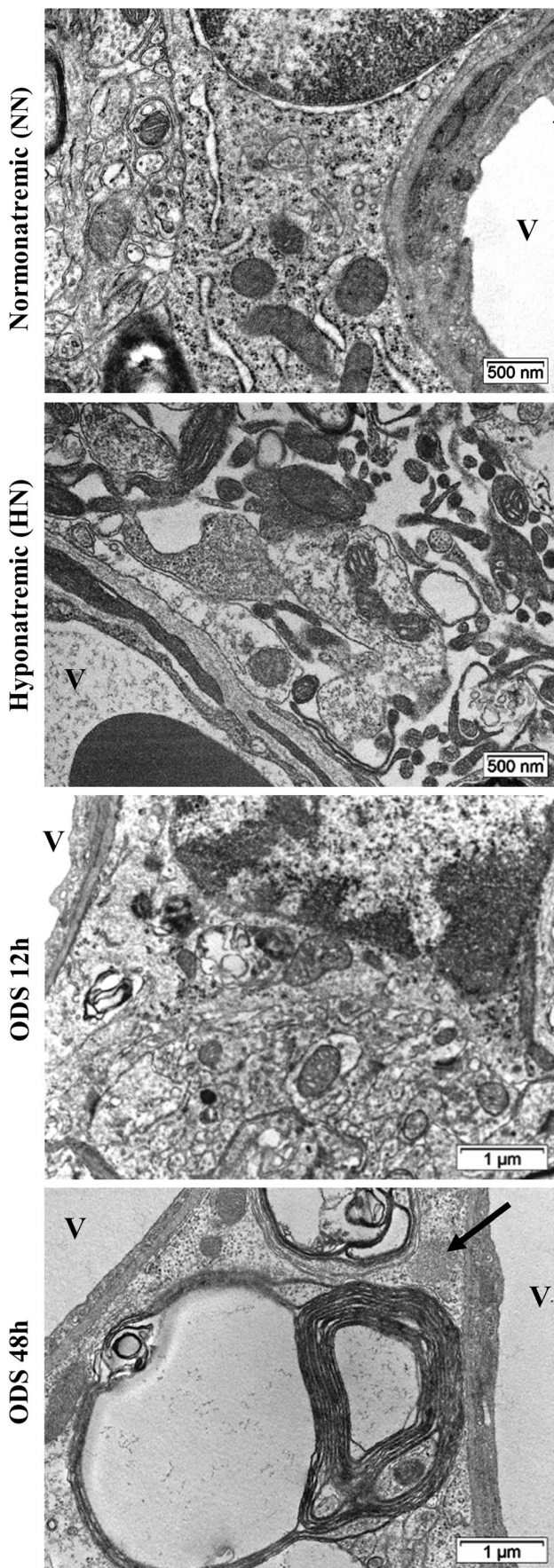


(Fig. 6d2, arrow). Distal extensions, associated with the perivascular zone of protoplasmic astrocytes, denoted poor organelle content save, some damaged endoplasmic reticulum, and sparse speckles of β -glycogen granules. The same aspect was seen in random sections of astrocytes of the adjacent neuropil. Throughout more than 30 grid fields, only a couple of cells were noted with a highly condensed nucleus containing by an extreme wavy, unevenly folded, filamentous-like packed chromatin with deep, complex entwined morphology. The cytoplasm had empty aspect, where only altered reticulum and rare mitochondria amongst strings of dot-contrasted β -glycogen granules contributed to make the degenerating astrocytes still identifiable between the surrounding fine structures of the neuropil, including synapses. However, the same field of view of Fig. 6e1 after enlargement show several demyelinated axons. One of such axonal demyelination is revealed by the enlarged view of Fig. 6e2, where an adjacent axon of the previously described altered astrocyte is fenced by its frothy myelin. Morphology alone could not decide about the type of cell death, but only preliminary data had suggested necroptosis, found in 12 h ODS oligodendrocytes and verified with immunohistochemical markers (Bouchat et al. 2018).

ODS 48 H Astrocytes from Perilesional Area Anti-GFAP immunolabeling allowed for an easy identification of the reactive astrocyte's area around the thalamic lesion (Supplemental Fig. S1). Ultrastructural analysis of the contralateral hemisphere confirmed astrogliosis in this area by finding enduring or healing remainder astrocytes, fairly enlarged, but displaying some organelle injuries, many lysosomal bodies and containing intermediate filaments (arrow in Fig. 8d), and many lysosomal and lipofuscin bodies. These cells are also bordered by cellular debris (arrowhead in Fig. 8c).

ODS 48 H Astrocytes from Caudate Putamen In order to strengthen these findings, the surveys of striatal astrocytes morphology found that no demyelinating lesions or cellular damages were noticed in the caudate putamen using light microscopy (Bouchat et al. 2018). To further confirm these data, our observations obtained in and around the ODS thalamus lesions were compared with a morphologically undamaged

Table 1 Morphological comparisons between surviving ODS 48 h astrocytes from lesion, perilesional gliotic area, and caudate putamen

	Lesion	Perilesional gliotic	Caudate putamen
Dilated organelles	+	+	+
Intermediate filaments	-	+	+
Cellular debris	-	+	-
Glycogen	Beta	Beta	Alpha

The plus sign indicates present; the minus sign indicates absent

central nervous system (CNS) area. As one would have expected, the ultrastructure analyses of astrocytes from the caudate putamen revealed an almost normal morphology with euchromatic nucleus and, in the perikaryon, short fascicles of typical 10–12 nm diameter intermediate filaments were found with high magnification (Fig. 8e, f). It is also possible that, even in this nerve tissue less susceptible towards osmotic shock, testing and processing had provoked minor dilatation of organelles such as those noted of the endoplasm cisterns (asterisk in Fig. 8f).

Electron microscopy analyses of the perivascular astrocyte end feet revealed some alterations after the correction of chronic hyponatremia. As noticed previously in the perikaryon of astrocytes (Fig. 6d1–2), patches of amassed and unidentified microfibrillar content were again discovered in ODS 48 h astrocyte extensions while endothelial cells and pericytes did not appear altered in our observations (Fig. 9). Swellings and alterations of astrocytes appeared to support what might cause changes in the BBB integrity.

Comparative observation of ODS 48 h surviving astrocytes from demyelinating lesion, perilesional area, and from the caudate putamen are summarized in Table 1 and also illustrated in Fig. 8.

Neurons

NN, HN, ODS 12 h, and ODS 48 h changes observed with LM at the nuclear level were comforted by ultrastructural observations because only some apparent minor alterations were revealed without apparent neuronal cell death (Fig. 10a1 for NN, 10b1 for HN, 10c1 for ODS 12 h, and 10d1 for ODS 48 h). Suggestive shrinking of HN and ODS 12 h neuronal cells with a nucleus bearing a highly compacted and round nucleolus (with particulate pre-RNAs) was noted. However, the neuropil was not emptied of ribosomes or RER (Fig. 10a2 for NN, 10b2 for HN, and 10c2 for ODS 12 h).

In ODS 48 h, neurons had a morphology that resembled the NN ones because cells contained not only a nucleus even more evidently indented than the NN neuron but also grooved (Fig. 10d1). Each nucleus was heavily decorated with nucleolar masses and the perikaryon neuropil compartment became jam-packed with polyribosomes, altogether suggesting a typical active transcription along with translation during the recovery from ODS challenge. This recovery was substantiated throughout because in all the ODS 48 h cells rough and smooth ER, active Golgi apparatus with heavily stacked saccules was viewed. Additionally, in some cells, a round body, 1–1.5 μm wide consisted in particles and fibrous aggregates. With a high magnification, one deciphered it to be made up entwined polyribosomes attached to their mRNA leaching out in the surrounding neuropil (Fig. 10d2).

Fig. 10 Representative ultrastructural aspects of NN, HN, ODS 12 h, and ODS 48 h thalamic neurons. Remarkably, HN neurons do not show deep nucleus indentation as in NN neurons (b1 vs. a1) and display lysosomal bodies (b2 vs. a2). ODS 12 h neurons revealed nuclei with more heterochromatin clearing and a cytoplasm with poor content of polyribosomes and rough endoplasmic reticulum (c1, c2) while ODS 48 h neurons demonstrate large, lightly indented euchromatic nuclei and huge amounts of neuropil polyribosomes (d1, d2); some adjacent damaged nerve fibers can still be noted (d1)

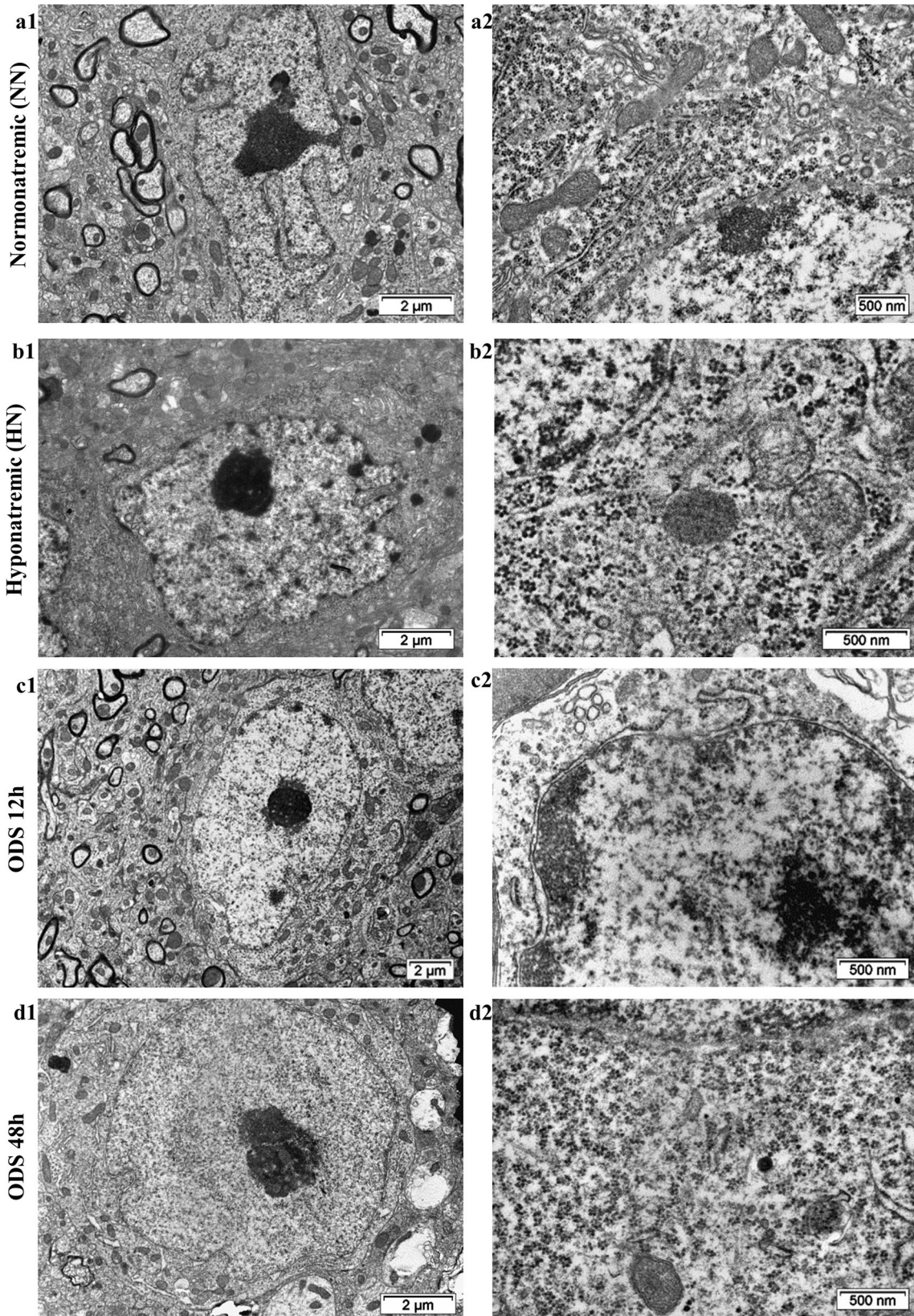
Microglial Cells

These quasi-flattened cells were difficult to compare between NN and HN groups but often recognized by their surrounding basal lamina, continuous with the basal lamina of the vessel's endothelium. Some of them contained variable amounts of lysosomes, even in the NN group (Fig. 11). However, ODS 12 h microglial cells evidently enlarged and the macrophagic activity became evident due to an abundant content of Golgi, multivesicular bodies, and accretion of electron-dense lysosomes of diverse sizes. This aspect was even more obvious in ODS 48 h because most of these cells filled the neuropil, loaded by debris engulfed through macrophagic activity. At this latest point surveyed, many subendothelial spaces (Fig. 11, ODS 48 h, asterisk) showed astrocyte debris, as swollen extensions containing scattered glycogen particles and havocs of membranes including myelin and other neuropil debris. In some lucky fields of view, some evident microglial cells with diverse heterogeneous lysosomal bodies extended by amoeboid trawling edges surface, crawling-like in the “clean” voids or cavities extending between neighboring interfascicular areas of the neuropil. There, hollowed spaces were probably created after the cell's degradations and damaged cell pieces have been removed since only tiny membrane debris could be seen remaining between these cells and the pericyte and endothelial cells (Fig. 11).

Discussion

Following the development of a mouse model of ODS induced by the abrupt correction of a chronic hyponatremia, analysis of fine structural aspects has been able to verify some neuropathologic damages previously described at the EM level (Bouchat et al. 2018). Many histopathologic similarities were found compared with the ODS rat model (Rojiani et al. 1994) and the human case studies (Powers and McKeever 1976).

During the chronic hyponatremia phase, all the macroglial cells examined at TEM showed stress-related adjustments imposed by the depleted osmotic environment. In general, oligodendrocytes and astrocytes contained wrinkled nucleus profiles and more compacted nucleolus than NN ones. Dilated



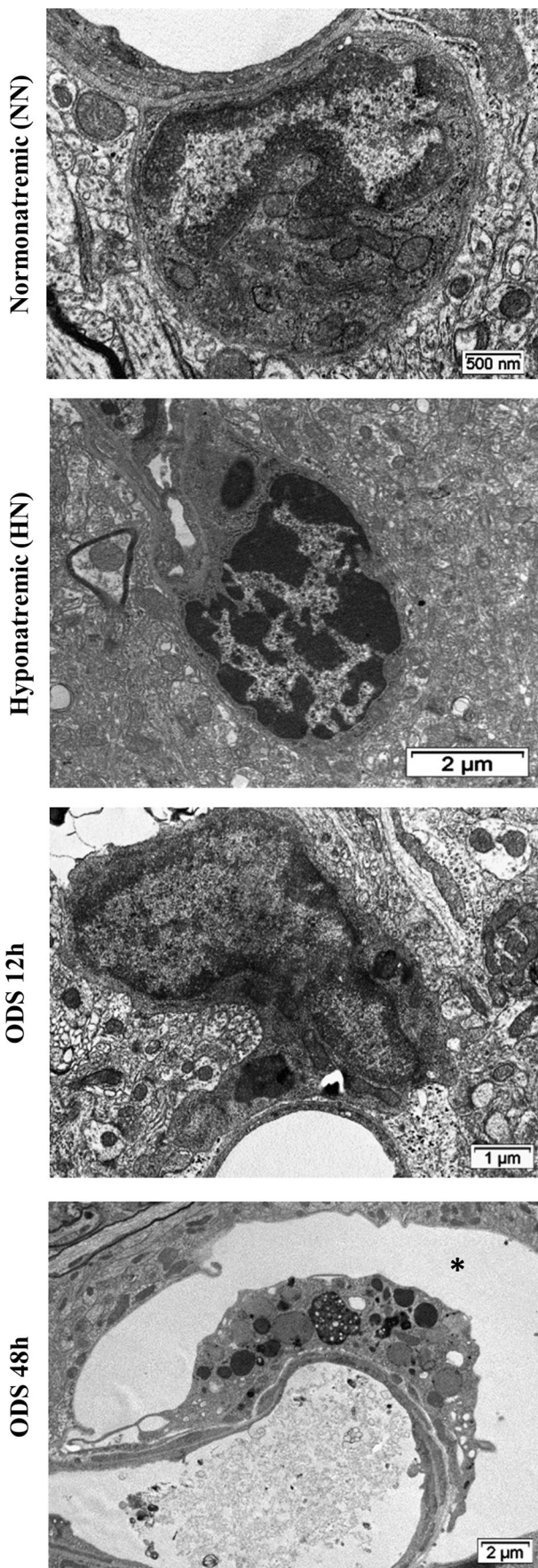
SER/RER cisterns and swollen mitochondria reflect the intracellular swelling caused by the influx of water from the extracellular space inside the glial cells. This water shift is likely most facilitated by aquaporin-specific water channel's expression of the astrocytes that help rerouting water selectively inside glial cells thereby sparing neurons from cytotoxic edema. In this setting, thalamic neurons were less changed, but nonetheless with a nucleus shape, getting rounder than in NN with blunted infoldings and displayed a reduced NeuN immunolabeling. Those neurons had dilated mitochondria among fields of innumerable free polysomes where the Golgi apparatus was more arduous to be found than in NN cells, but these minor defects and organelles were easily found again as soon as the hyponatremia ceased. These cytological evidences and marker pattern changes seemed comforted by the compacted nucleolus aspect and reduction of translational activities (Gusel'nikova and Korzhevskiy 2015).

Once correction of hyponatremia was initiated, degradative morphological changes were observed in the thalamic glial cells once correction of hyponatremia was initiated. Twelve hours after a rapid correction of hyponatremia, the survey of semi-thin sections revealed oligodendrocytes nuclei with strong toluidine blue staining pattern that display a peripheral heterochromatin accumulation with a tiny central nucleolus mass. This pattern corresponded with the highest electron contrast noted in the ultrastructure. Such chromatin modifications have already been described as “chromatin clumping” by Rojiani (1994). In addition to the thick layer of heterochromatin lining the nuclear envelope, an associated mottled contrast revealed in its continuity did not appear revealed with the toluidine blue stain, suggesting other modifications of the nucleoplasm concerning the chromatin compaction and the appearance of interchromatin granules suggesting a pause in transcription and translation along with a breakdown of the nucleolus reduced to a small bunch of ribosomal precursors (Derenzini et al. 2006; Scheer et al. 1993; Thiry et al. 1997). Compared among all oligodendrocytes, the strongest to lowest heterochromatin contrast sequence was estimated qualitatively as: ODS 12 h > ODS 48 h > HN \geq NN. This accumulated oligodendrocyte heterochromatin, in continuity with a lesser but still electron-contrasted hue zone of the ODS 12 h oligodendrocyte nucleoplasm, was accompanied by a perikaryon and further distal cytoplasm that contained small rimmed vacuoles and mitochondria profiles with a swollen matrix while scattered free ribosomes remained as well as rough endoplasmic structures. During ODS challenge and afterwards, most of the glial cells seemed to survive and retrieved a transcriptional activity while, in some cases, and for unclear causes, cells injured were undergoing a form of cell death. The nuclear condensation herein reported could also be related to the initiation of a nuclear elimination program after irreversible cell injury, set during an alternative programmed cell death. Apoptosis or necrosis was excluded in favor of necroptosis

Fig. 11 Representative ultrastructural aspects of NN, NH, ODS 12 h, and ODS 48 h thalamus microglial cells. Recognized from almost round to spindle cells, showing a small irregularly lobed nucleus in NN microglial cells. HN and ODS microglial cells contain diverse content of lysosomal bodies adjacent of small to large cavernous spaces (ODS 12 h and asterisk in ODS 48 h) caused by the clearing of myelin, axons, and excised corpse's pieces of macroglial cell's remains (in the sequence ODS 48 h > ODS 12 h > HN), thus showing that some sub-vascular regions bore tissue fragilization that would result in a poor physiologic support of the blood-brain barrier now left with a flimsy endothelium and pericyte lining

given the absence of ultrastructural clues such as nuclear fragmentation with formation of apoptotic bodies or nucleus swelling with chromatin clearing, ruptured cell membranes, and nuclear envelope remaining to occur at once. The micrographs submitted are also unique because necroptosis is a recent discovery (Vanden Berghe et al. 2010) and has been seldom illustrated with ultrastructure but with the use of in vitro cell lines (Belizario et al. 2015; Chen et al. 2018; Nomura et al. 2014). Our data best correspond with those found in Belizário and others (Belizario et al. 2015) and reviewed in Zhou and Yuan (2014) where Wang et al. (2012) support for this mode of death cell demise in the CNS. There, severely injured glial cells with a critical plasma membrane dissolution-like along with that of organelles liberate into large chromatin condensates, as hallmarks of necroptosis with specific positive molecular markers indicating a cell death through necroptosis (Bouchat et al. 2018; Croker et al. 2018).

ODS astrocytes also showed a more electron-contrast cytoplasm than typical with peculiar swelling of the endoplasmic reticulum and whatever damages they underwent were carried on using glycolysis because the glycogen reserves that were detected scattered have been β -glycogen granule form (Bak et al. 2018; Maxwell and Kruger 1965) indicating and comforting a glycolytic activity support and exchange with the adjacent cells, including the oligodendrocytes. Furthermore, electron microscopy observations have also validated previous suggestions of clasmatodendrosis of the astrocyte extensions and end feet fragilized among the neuropil and disruptions of their intercellular contacts. Although gap junctions between astrocytes were maintained, astrocyte-oligodendrocyte (A/O) junctions were disrupted and were associated with the unilateral compaction of dense submembranous components in the astrocyte, adjacent to oligodendrocyte contact. The nature of such altered junction remains unidentified (Morales and Duncan 1975). Dysregulation of A/O gap junctions caused demyelination, as demonstrated by Cx47 and Cx30/Cx43 knock-down mouse models (Lutz et al. 2009; Odermatt et al. 2003). Astrocyte distal processes cannot be passive architectural elements because of active mRNA and protein synthesis with a reactivation of an apparent functional sorting machinery (ribosomes, endoplasmic reticulum, and Golgi



apparatus). The production of transmembrane or secreted proteins at the astrocyte end feet sustains for instance the functional polarization of the gliovascular interface (Boulay et al. 2017; Sakers et al. 2017). Therefore, removing such fundamental biological processes would lead undoubtedly to gliovascular defects and to BBB dysfunction, as observed in the course of ODS at latter time points (Adler et al. 2000; Baker et al. 2000; Bouchat et al. 2018; Gankam Kengne et al. 2011). In astrocytes, the cell architecture and polarization largely rely on the cytoskeleton integrity; therefore, disturbing GFAP homeostasis and/or organization might contribute to cell dislocation and loss of cell contact at the most distal extensions. Our ultrastructural analysis proved that intermediate filaments were destabilized and further suggests that the osmotic stress could provoke their faulty proteinaceous aggregates in the astrocyte perikaryon and end feet. These fibrillary components could be formed by intermediate filaments alone or associated with other macromolecules, and/or with other microfilaments. In order to identify the nature of these aggregates, GFAP and actin immunogold labelling were assayed. However, these labellings failed to identify cytoskeleton elements. It is possible that precursors of GFAP have been present with presenting antigenic sites hidden in the bulk of as mixed filamentous, unprocessed microscopic feature arrested, caused by the osmotic stress and retrieval of other metabolic demands for other repairs. The nucleolus structure disturbances and switched metabolic glycolysis (residual dispersed β -glycogen) could mirror cells under ODS restoration keeping with only essential maintenance along with some autophagocytoses (clasmotodendrosis). A delayed turn-over in translations or of some cytoplasmic post-translational modifications in protein processing may have been hindered causing cytoplasmic deposits that may encompass the uncompleted cytoskeleton. If among them were GFAP precursors, their faulty folding and/or incomplete antigenic sites positioning would have thus interfered with any possible antibody recognition binding. Furthermore, a recent report mentioned proteostasis disturbances in astrocytes of ODS-susceptible regions (Gankam-Kengne et al. 2017). Gankam and coll. showed that upon correction of hyponatremia, brain astrocytes rapidly accumulated ubiquitin-tagged insoluble and aggregated proteins in their perikaryon. Using another set of molecular markers, they suggested that osmotic stress induced the unfolded protein response and ER stress response in those astrocytes. Activation of these pathways is linked to increased expression of ER resident chaperones that can lead, in astrocytes, to clasmotodendrosis, or even cell death in case of sustained over activation (Kim et al. 2017; Xu et al. 2005). SER dilatation and vacuoles observed in our samples could be linked to this dysregulated proteostasis during osmotic stress. Dilatation of neuronal ER could also precede necroptosis as described by Chavez-Valdez and coll. in 2016 in a model of neonatal hypoxia-ischemia. They observed early changes in neurons characterized by ER dilatation and mitochondria swelling.

Only thalamus ODS 48 h astrocytes within demyelinating lesion presented morphological major alterations, while ODS 48 h astrocytes from the caudate putamen only showed insignificant dilations of the endoplasmic cisterns and no nucleus or intermediate filament's changes. An astrogliosis arose around the thalamic lesion and revealed reactive astrocyte's morphology consisting in organelle's autophagy intracytoplasmic cell debris, lysosomes, and lipofuscin bodies with presence of intermediate filaments. This astrogliosis has already been described in several publications about ODS in human or in animal models in light microscopy but has never been shown in ultrastructure analysis.

In conclusion, this study has been able to confirm that, as a result of rapid correction of chronic hyponatremia, morphological changes found in the murine thalamus consist in: (a) Regional demyelination of axons at 48 h post-correction, followed by the removal of cell debris, myelin, or damaged neural content; (b) most oligodendrocytes show a peculiar hyperchromatic aspect, retrieving their normal aspects at 48 h surviving out of “desperate” glycolysis; concomitantly, a few damaged ones undergo cell death at 12 h post-correction; (c) astrocytes changes consist in nuclear shrinking and undergo clasmotodendrosis while some of them retrieve an active and normal morphology after 48 h. Additionally at 12 and 48 h after correction, astrocytes contain large intracytoplasmic aggregates of undetermined content in the perikaryon but also in end feet which could be implicated in BBB defects; (d) neurons show plasticity demonstrating a main nuclear shutdown of transcription at 12 h while at 48 h, enormous amounts of perikaryal polyribosomes reveal that transcription is reactivated along with translation; and (e) microglial cells appear to have managed removal of myelin debris or astrocyte corpses, leaving many subendothelial and interfascicular empty spaces that could likely fragilize the adjacent neuropil and become supplemental sources of breaking loci of the BBB at later time points. These results corroborated those obtained by previous teams using electron microscopy to unravel ODS physiopathology in human and in the rat model, namely oligodendrocytes presenting signs of degeneration but not death and presence of living astrocytes in lesion at 48 h after the correction (Powers and McKeever 1976; Rojiani et al. 1994).

Acknowledgments We are grateful to C. Charlier and C. De Bona for their technical support. This research used the Electron Microscope facility of the “Plateforme Technologique Morphologie–Imagerie” of UNamur.

Funding J.P.B was supported by grants from the Belgian “Fonds de la Recherche Scientifique Médicale” (T.0023.15) and the Belgian Foundation “Recherche Alzheimer/ Stichting Alzheimer Onderzoek” (14001) (Fund Aline).

Compliance with Ethical Standards

The experimental protocol was conducted in compliance with the European Communities Council Directives for Animal Experiments (2010/63/EU, 87-848/EEC and 86/609/EEC) and was approved by the

Animal Ethics Committee of University of Namur (Ethic project n°14-210).

References

- Adams RD, Victor M, Mancall EL (1959) Central pontine myelinolysis: a hitherto undescribed disease occurring in alcoholic and malnourished patients. *AMA Arch Neurol Psychiatry* 81:154–172
- Adler S, Verbalis JG, Meyers S, Simplaceanu E, Williams DS (2000) Changes in cerebral blood flow and distribution associated with acute increases in plasma sodium and osmolality of chronic hyponatremic rats. *Exp Neurol* 163:63–71
- Bak LK, Walls AB, Schousboe A, Waagepetersen HS (2018) Astrocytic glycogen metabolism in the healthy and diseased brain. *J Biol Chem* 293:7108–7116
- Baker EA, Tian Y, Adler S, Verbalis JG (2000) Blood-brain barrier disruption and complement activation in the brain following rapid correction of chronic hyponatremia. *Exp Neurol* 165:221–230
- Belizario J, Vieira-Cordeiro L, Enns S (2015) Necroptotic cell death signaling and execution pathway: lessons from knockout mice. *Mediat Inflamm* 2015:128076
- Bouchat J, Couturier B, Mameffe C, Gankam-Kengne F, Balau B, De Swert K, Brion JP, Poncelet L, Gilloteaux J, Nicaise C (2018) Regional oligodendrocytopathy and astrocytopathy precede myelin loss and blood-brain barrier disruption in a murine model of osmotic demyelination syndrome. *Glia* 66:606–622
- Boulay AC, Saubamea B, Adam N, Chasseigneaux S, Mazare N, Gilbert A, Bahin M, Bastianelli L, Blugeon C, Perrin S et al (2017) Translation in astrocyte distal processes sets molecular heterogeneity at the gliovascular interface. *Cell Discov* 3:17005
- Chen D, Tong J, Yang L, Wei L, Stolz DB, Yu J, Zhang J, Zhang L (2018) PUMA amplifies necroptosis signaling by activating cytosolic DNA sensors. *Proc Natl Acad Sci U S A* 115:3930–3935
- Crocker B, Rickard J, Shlomovitz I, Al-Obeidi A, D’Cruz A, Gerlic M (2018) Necroptosis. In: Radosevich JA (ed) *Apoptosis and beyond: the many ways cells die*. Wiley-Blackwell, Hoboken, pp 99–126
- Derenzini M, Pasquinelli G, O’Donohue MF, Ploton D, Thiry M (2006) Structural and functional organization of ribosomal genes within the mammalian cell nucleolus. *J Histochem Cytochem* 54:131–145
- Gankam Kengne F, Nicaise C, Soupart A, Boom A, Schiettecatte J, Pochet R, Brion JP, Decaux G (2011) Astrocytes are an early target in osmotic demyelination syndrome. *J Am Soc Nephrol* 22:1834–1845
- Gankam-Kengne F, Couturier BS, Soupart A, Brion JP, Decaux G (2017) Osmotic stress-induced defective glial proteostasis contributes to brain demyelination after hyponatremia treatment. *J Am Soc Nephrol* 28:1802–1813
- Gocht A, Lohler J (1990) Changes in glial cell markers in recent and old demyelinated lesions in central pontine myelinolysis. *Acta Neuropathol* 80:46–58
- Gusel’nikova VV, Korzhhevskiy DE (2015) NeuN as a neuronal nuclear antigen and neuron differentiation marker. *Acta Nat* 7:42–47
- Illowsky BP, Laureno R (1987) Encephalopathy and myelinolysis after rapid correction of hyponatraemia. *Brain* 110(Pt 4):855–867
- Kim JE, Hyun HW, Min SJ, Kang TC (2017) Sustained HSP25 expression induces clasmotodendrosis via ER stress in the rat hippocampus. *Front Cell Neurosci* 11:47
- Kleinschmidt-DeMasters BK, Norenberg MD (1981) Rapid correction of hyponatremia causes demyelination: relation to central pontine myelinolysis. *Science* 211:1068–1070
- Laureno R (1983) Central pontine myelinolysis following rapid correction of hyponatremia. *Ann Neurol* 13:232–242
- Lutz SE, Zhao Y, Gulino M, Lee SC, Raine CS, Brosnan CF (2009) Deletion of astrocyte connexins 43 and 30 leads to a dysmyelinating

- phenotype and hippocampal CA1 vacuolation. *J Neurosci* 29:7743–7752
- Maxwell DS, Kruger L (1965) The fine structure of astrocytes in the cerebral cortex and their response to focal injury produced by heavy ionizing particles. *J Cell Biol* 25:141–157
- Morales R, Duncan D (1975) Specialized contacts of astrocytes with astrocytes and with other cell types in the spinal cord of the cat. *Anat Rec* 182:255–265
- Nomura M, Ueno A, Saga K, Fukuzawa M, Kaneda Y (2014) Accumulation of cytosolic calcium induces necroptotic cell death in human neuroblastoma. *Cancer Res* 74:1056–1066
- Odermatt B, Wellershaus K, Wallraff A, Seifert G, Degen J, Euwens C, Fuss B, Bussow H, Schilling K, Steinhauser C et al (2003) Connexin 47 (Cx47)-deficient mice with enhanced green fluorescent protein reporter gene reveal predominant oligodendrocytic expression of Cx47 and display vacuolized myelin in the CNS. *J Neurosci* 23:4549–4559
- Popescu BF, Bunyan RF, Guo Y, Parisi JE, Lennon VA, Lucchinetti CF (2013) Evidence of aquaporin involvement in human central pontine myelinolysis. *Acta Neuropathol Commun* 1:40
- Powers JM, McKeever PE (1976) Central pontine myelinolysis. An ultrastructural and elemental study. *J Neurol Sci* 29:65–81
- Rojiani AM, Cho ES, Sharer L, Prineas JW (1994) Electrolyte-induced demyelination in rats. 2. Ultrastructural evolution. *Acta Neuropathol* 88:293–299
- Sakers K, Lake AM, Khazanchi R, Ouwenga R, Vasek MJ, Dani A, Dougherty JD (2017) Astrocytes locally translate transcripts in their peripheral processes. *Proc Natl Acad Sci U S A* 114:E3830–E3838
- Scheer U, Thiry M, Goessens G (1993) Structure, function and assembly of the nucleolus. *Trends Cell Biol* 3:236–241
- Thiry M, Jamison JM, Gilloteaux J, Summers JL, Goessens G (1997) Ultrastructural nucleolar alterations induced by an ametantrone/polyr(A-U) complex. *Exp Cell Res* 236:275–284
- Tomlinson BE, Pierides AM, Bradley WG (1976) Central pontine myelinolysis. Two cases with associated electrolyte disturbance. *Q J Med* 45:373–386
- Vanden Berghe T, Vanlangenakker N, Parthoens E, Deckers W, Devos M, Festjens N, Guerin CJ, Brunk UT, Declercq W, Vandenaabeele P (2010) Necroptosis, necrosis and secondary necrosis converge on similar cellular disintegration features. *Cell Death Differ* 17:922–930
- Verbalis JG, Drutarosky MD (1988) Adaptation to chronic hyposmolality in rats. *Kidney Int* 34:351–360
- Wang YQ, Wang L, Zhang MY, Wang T, Bao HJ, Liu WL, Dai DK, Zhang L, Chang P, Dong WW et al (2012) Necrostatin-1 suppresses autophagy and apoptosis in mice traumatic brain injury model. *Neurochem Res* 37:1849–58
- Xu C, Bailly-Maitre B, Reed JC (2005) Endoplasmic reticulum stress: cell life and death decisions. *J Clin Invest* 115:2656–2664
- Zhou W, Yuan J (2014) Necroptosis in health and diseases. *Semin Cell Dev Biol* 35:14–23

Publisher's Note Springer Nature remains neutral with regard to jurisdictional claims in published maps and institutional affiliations.